Soft Matter

Relative effects of polymer composition and sample preparation on glass dynamics

Journal:	*Soft Matter*
Manuscript ID	SM-COM-05-2022-000698.R2
Article Type:	Communication
Date Submitted by the Author:	13-Aug-2022
Complete List of Authors:	Elder, Robert M.; U.S. Food and Drug Administration, Center for Devices and Radiological Health Forster, Amanda; National Institute of Standards and Technology, Materials Measurement Science Division Krishnamurthy, Ajay ; National Institute of Standards and Technology, Materials Measurement Science Division Dennis, Joseph; U.S. DEVCOM Army Research Laboratory, Polymers Branch Akiba, Hiroshi; University of Tokyo, Institute for Solid State Physics Yamamuro, Osamu; University of Tokyo, Institute for Solid State Physics Ito, Kanae; Japan Synchrotron Radiation Research Institute, Industrial Application Division, Spring-8 Evans, Katherine; National Institute of Standards and Technology, Materials Science and Engineering Division Soles, Christopher; National Institute of Standards and Technology, Materials Science and Engineering Division Sirk, Timothy; U.S. DEVCOM Army Research Laboratory, Polymers Branch

Soft Matter

ARTICLE TYPE

Cite this: DOI: 00.0000/xxxxxxxxxx

Relative effects of polymer composition and sample preparation on glass dynamics

Robert M. Elder[a*], Amanda L. Forster[b], Ajay Krishnamurthy[b], Joseph M. Dennis[c], Hiroshi Akiba[d], Osamu Yamamuro[d], Kanae Ito[e], Katherine M. Evans[f], Christopher Soles[f], Timothy W. Sirk[c*]

Received Date
Accepted Date

DOI: 00.0000/xxxxxxxxxx

Modern design of common adhesives, composites and polymeric parts makes use of polymer glasses that are stiff enough to maintain their shape under a high stress while still having a ductile behavior after the yield point. Typically, material compositions are tuned with co-monomers, polymer blends, plasticizers, or other additives to arrive at a tradeoff between the elastic modulus and toughness. In contrast, strong changes to the mechanics of a glass are possible by changing only the molecular packing during vitrification or even deep in the glassy state. Conversely, physical aging or processing techniques such as physical vapor deposition increase the density, embrittle the material, and increase elastic modulus. Here, we use molecular simulations, validated by positron annihilation lifetime spectroscopy and quasi-elastic neutron scattering, to understand the free volume distribution and the resulting dynamics of glassy co-polymers where the composition is systemically varied between polar 5-norbornene-2-methanol (NBOH) and non-polar ethylidene norbornene (ENB) monomers. In these polymer glasses, we analyze the structural features of the unoccupied volume using clustering analysis, where the clustering is parameterized to reproduce experimental measurements of the same features from positron annihilation spectroscopy (PALS). Further, we analyze the dynamics, quantified by the Debye-Waller factor, and compare the results with softer, lower density states. Our findings indicate that faster structural relaxations and potentially improved ductility are possible through changes to the geometric structure and fraction of the free volume, and that the resulting changes to the glass dynamics are comparable to large changes in the monomer composition.

In this work, we use molecular simulations and experiments to examine the relationship of the molecular packing, as quantified by size and shapes of voids ("holes"), with the dynamics of polar and non-polar polymer glasses. In particular, we compare the relative effect of the glass structure, which is controlled by material processing, with the choice of monomer composition. Polymer chemistries based on 5-norbornene-2-methanol (NBOH) and a related monomer, ethylidene norbornene (ENB) were considered. NBOH contains a polar hydroxy group capable of hydrogen bonding, whereas ENB is entirely non-polar. The level of polar chemistry was systematically varied by adjusting the number of NBOH and ENB monomers in the chains; The most polar chemistry is pure NBOH (termed 0% ENB), while the least polar is pure ENB (termed 100% ENB). Intermediate polarities are represented by ENB-*co*-NBOH copolymers termed 25, 50, and 75% ENB to denote the ENB fraction. In the simulations, each polymer chain contains a fixed number of 20 ENB or NBOH monomers, resulting in a chain molecular mass that is approximately constant. Likewise, the chains have similar flexibility, an important factor for nanovoids,[1,2] which we verified by calculating the backbone orientational correlation and the persistence length. These compositions and their properties are summarized in Table 1. Molecular structures were created above the glass transition temperature (Tg), equilibrated, and quenched into the glassy state at 300 K at a quench rate of 10^{11}, 10^{12}, or 10^{13} K/s, along with another set

[a]*current address: Center for Devices and Radiological Health, U.S. Food and Drug Administration, Silver Spring, Maryland 20903, United States; E-mail: robert.elder@fda.hhs.gov*
[b]*Materials Measurement Science Division, National Institute of Standards and Technology, Gaithersburg, Maryland 20899, United States*
[c]*Polymers Branch, U.S. DEVCOM Army Research Laboratory, Aberdeen Proving Ground, Maryland 21005, United States; E-mail: timothy.w.sirk.civ@army.mil*
[d]*Institute for Solid State Physics, University of Tokyo, Kashiwa, Chiba, 277-8581, Japan*
[e]*Industrial Application Division, Spring-8, Japan Synchrotron Radiation Research Institute (JASRI), 1-1-1 Kouto, Sayo, Hyogo 679-5198, Japan*
[f]*Materials Science and Engineering Division, National Institute of Standards and Technology, Gaithersburg, Maryland 20899, United States*
† Electronic Supplementary Information (ESI) available: Additional details and data for molecular simulations and experiments.

of structures, nominally labeled 10^0 K/s, that were generated at the experimental density. As discussed below, the density changes that are introduced by varying the quench rate greatly effect the local molecular dynamics, as density is a strong indicator of glass dynamics such as the Debye-Waller factor.[3,4] Further simulation details and analysis are given in the ESI.

Experimental samples of the same compositions were synthesized as described in prior work,[5] followed by analysis with positron annihilation lifetime spectroscopy (PALS) and quasi-elastic neutron scattering (QENS). PALS uses positrons to probe spatial packing deficiencies or density heterogeneities in the material at the sub-nanometer scale. While the voids identified by PALS are sometimes referred to as "free volume", they can either be static (as in a zeolite) or dynamic (as in a liquid) in nature. In polymers, voids usually consist of both static and dynamic packing defects.[6] The positron source, a radioactive salt, is placed between two pieces of the material of interest so that positrons are injected into the material. These injected positrons eventually thermalize and pick up a free electron to form the positronium bound state. The electron-positron pair is a neutral bound state, with a diameter comparable to an H atom. The parallel-spin triplet state, known as ortho-positronium (o-Ps) is long lived with a 142 ns lifetime in a vacuum. However, in polymers the neutral o-Ps lifetime (τ_3) is cut short by the pick-off annihilation mechanism, typically on the order of 1 to 10 ns. As o-Ps is a neutral species, it minimizes interactions with the material and localizes in low density regions of the sample. Empirical calibrations with zeolites and other controlled-pore solids are used to correlate τ_3 with hole size. The positron hole size is typically calculated using the semi-empirical Tau-Eldrup equation, $\tau_3 = \frac{1}{2}\left[1 - R/(R+0.166) + \sin\left(2\pi R/(R+0.166)\right)/2\pi\right]^{-1}$ with corresponding hole (void) volume $\langle V_v \rangle = (4/3)\pi R^3$.[7] Further details are given elsewhere.[8] The mean-square displacements (MSD) for compositions $\phi_{ENB} = 0$, 50 and 100 were quantified using the elastic intensities from quasi-elastic neutron scattering (QENS) measurements, performed on the Angle Focusing Cold Neutron Spectometer[9] (AGNES) installed by the Institute for Solid State Physics, University of Tokyo, at Japanese Research Reactor 3 (JRR-3), Japan Atomic Energy Agency (JAEA), in Tokai, Japan. Measurements of the MSD represent a time range spanning approximately 10 ps for a series of temperatures, including 300 K. Details are given in the ESI.

Parameterization of simulated voids with PALS data. Voids were identified from molecular structures as follows: (1) Unoccupied volume was found by overlaying a cubic grid on the atomic coordinates (0.5 Å grid resolution); Any grid points overlapping an atomic van der Waals radius were taken as occupied voxels. The remaining unoccupied grid points (i.e., empty voxels) were further processed in the following step. (2) Voids were identified as large contiguous groups of empty voxels using the Density-Based Spatial Clustering of Applications with Noise (DBSCAN) algorithm.[10,11] DBSCAN identifies discrete regions of high density (clusters) and regions of low density (outliers); Empty voxels were characterized in this way as belonging to either larger and more consolidated "void spaces" (clusters) or small "interstitial spaces" (outliers). The density metric is defined through two parameters, which are the neighborhood radius ε and the minimum number of neighborhood points M. A simple demonstration of the algorithm for a two-dimensional cartoon is given in Fig. 1. In molecular simulations, we selected a single set of parameters, $\varepsilon = 2.58$ Å and $M = 260$, by matching the average void volume from 5 replica simulations taken at the experimental mass densities with the PALS hole volume, where only the simulation data for $\phi_{ENB} = 0$ was considered. Examples of individual voids are given in Fig. 2a. As shown in Figure 2b, excellent agreement is obtained between the PALS data and simulations across all five of the compositions using a single set of parameters derived from $\phi_{ENB} = 0$.

We note that previous comparisons of simulations with PALS hole volumes suggest that a minimum void size should be imposed on the MD data.[12] A likely reason is that small voids in static MD snapshots are dynamically filled more rapidly than the time-scale τ_3 of a PALS measurement, and therefore cannot contribute to the PALS hole volume. Our approach using clustering analysis introduces an approximate, though not absolute, mini-

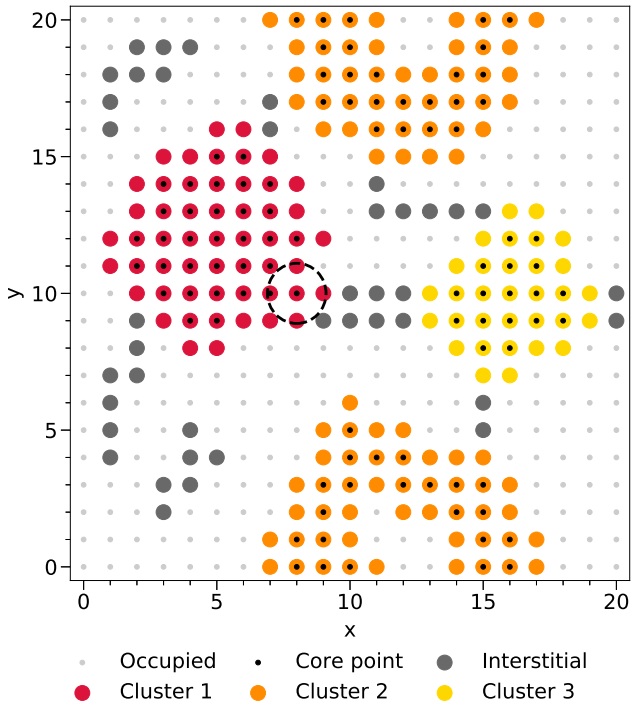

Fig. 1 A two-dimensional cartoon of the void identification algorithm acting on a single snapshot. A grid is superimposed on the atomic coordinates (not shown); Occupied grid points (small gray circles) are discarded; Unoccupied points (large circles) are analyzed by a clustering algorithm. Points with at least M neighbors within a radius ε are 'core points' (color circles with black dots) with $M = 4$ and $\varepsilon = 1.1$ taken for this example. The dashed black circle shows the neighborhood of one core point. Neighboring core points are assigned to the same cluster, along with their neighbors, which may have fewer than M neighbors (no black dots). Outliers (large gray circles) are points that do not belong to any cluster. This algorithm can recognize irregular geometries and account for periodic boundaries (orange Cluster 2). In the main text, clusters of unoccupied space are termed 'voids' while the outliers are termed 'interstitial' spaces.

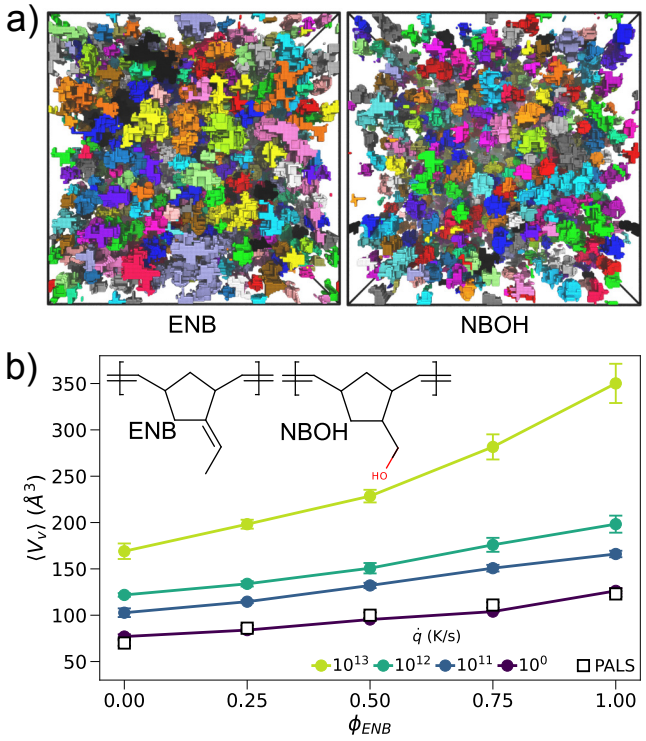

Fig. 2 (a) Representative snapshots of voids (colored shapes) in ENB and NBOH. The atoms and interstitial spaces are not shown. (b) The average volume of individual voids $\langle V_v \rangle$ vs. quench rate $\dot{q}$ and composition ϕ_{ENB} for simulations and as found from PALS experiments. Inset: monomer chemistries studied in this work.

mum size for cavities through the minimum number of neighbors M. Using the parameters above, the minimum cavity size is the product of $M = 260$ and the voxel volume (0.5 Å)^3, corresponding to a void volume of 32.5 Å^3. Voids of the minimum size as well as a handful of smaller voids, ∼10-20 per structure, appear due to the sequential nature of the clustering algorithm (see Fig. S2 of the ESI).*

Table 1 Summary of compositions (ϕ_{ENB}) and properties used to match simulations with PALS data. Each composition contains N_{NB} NBOH monomers and N_{ENB} ENB monomers per chain with exactly 136,000 total atoms at inverse mass density $\hat{v}$. The polarity and Debye-Waller factor $\langle u^2 \rangle$ are taken from the normalized octanol-water partition coefficient and mean square displacements, respectively, as detailed in the ESI.

ϕ_{ENB}	N_{ENB}	N_{NB}	$\hat{v}$, cm^3/g	$\langle u^2 \rangle$, Å^2	polarity, nm^{-2}
0	0	20	0.916	0.48	0.29
25	5	15	0.945	0.57	0.28
50	10	10	0.974	0.66	0.25
75	15	5	1.003	0.75	0.21
100	20	0	1.038	0.85	0.16

Discussion. Below Tg, differences in the free volume develop due to either the chemical composition or external influences such as the quench rate, confinement effects, or perturbations that prevent packing. Thus, both compositional changes and processing are possible routes to tailor the rheology and mechanics for specific needs. Intuitively, either of these changes would be expected to strongly alter the mechanics below Tg through changes to the character of segmental relaxations, such as the spatial extent of rearrangements in non-linear mechanics. Indeed, the literature shows that the yield and toughness of model thermoplastics are tunable through acceleration or damping of the segmental dynamics[16], where increased segmental motion has been linked with the collapse of voids that would otherwise initiate crazing[17]. For example, in recent work Soles et al. measured the MSD of polycarbonate materials with QENS, showing that the Debye-Waller $\langle u^2 \rangle$ factor, as well as slower diffusive modes, are correlated with material toughness.[18,19] However, the segmental dynamics and resulting material properties cannot be simply reduced to functions of only the free volume, as it is widely understood that moving along an isochoric (constant volume) path by varying pressure and temperature does not, in general, preserve the dynamics. Therefore, relationships that link composition and processing to dynamics are particularly relevant since these invoke different challenges in material design. Strong compositional changes can undermine the compatibility of the polymer matrix with fillers, fibers, sheets, and their sizing packages in composite materials, whereas changes to the glass packing with processing can be expected to introduce new relaxations and potentially accelerate ageing, densification, and embrittlement. These effects have been demonstrated by altering the density[20] of polymeric glasses such as in physical vapor deposition[21] and pulsed laser ablation[22].

The full structural relaxation of a glass cannot be measured with explicit molecular simulations due to the mismatch of the physical timescale with molecular dynamics. We leverage localization models that allow an estimate of the glass structural relaxation time τ to be constructed from the relatively small lengths and brief dynamics available to simulations. Such models capture the emergent behavior of time- and spatially-extended relaxations from the faster cage-rattling motions. An early prediction of a relaxation time v_f from the 'free volume' available for molecular motion was proposed by Turnbull and Cohen[23] for glass formers near the glass transition as $\log(\tau/\tau_0) = v_0/v_f$. As described below, we leverage this expression well below the T_g, nominally in the range of $T/T_g \approx 0.77$; example data for $T > T_g$ is given for comparison in the ESI (Fig. S6). Separately, in glassy materials, τ was linked with Debye-Waller factor $\langle u^2 \rangle$ by Hall and Wolynes[24], therefore implying a relation between $\langle u^2 \rangle$ with v_f. Dimensional analysis arguments[25,26] indicate that Debye-Waller factor is proportional to spherical free volume cavities as $v_f \sim \langle u^2 \rangle^{3/2}$. More generally, Simmons et al. have shown a proportional relation can be expected to hold provided that the structural features of the free volume, such as the population of free volume shapes, is preserved.[26] For non-spherical shapes, the proportionality becomes

$$v_f \sim \langle u^2 \rangle^{\alpha/2}, \quad (1)$$

* Specifically, a small number of voxels have the potential to belong to more than one cluster. Because voxels are assigned to the earliest cluster that can claim them, the particular order of voxel assignments occasionally causes clusters, some of which would have been near the minimum size of 260 voxels, to lose a small number of voxels to competing clusters.

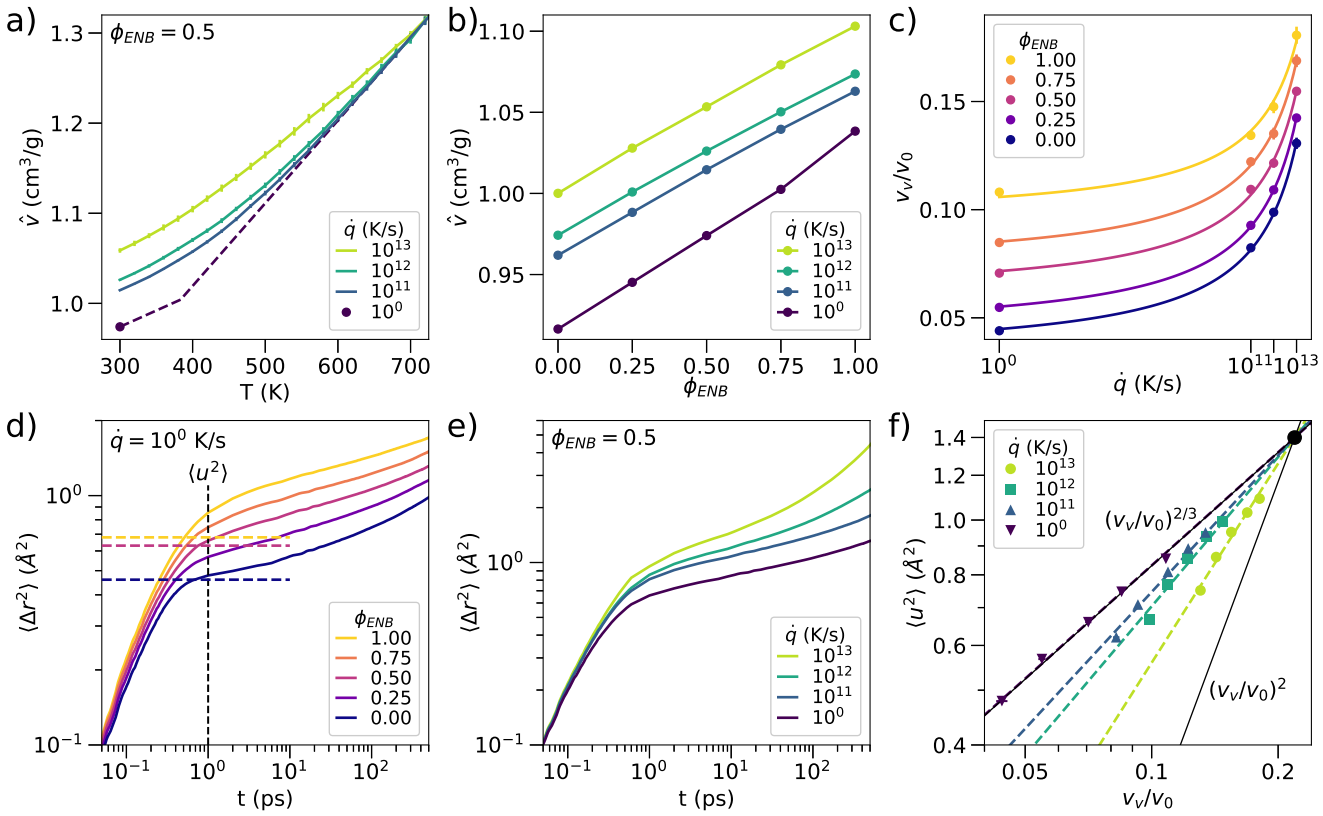

Fig. 3 Overview of volumetric and dynamical properties from MD simulations. a) Specific volume $\hat{v}$ and temperature T diagram at each cooling rate $\dot{q}$ for a representative composition of $\phi_{ENB} = 0.5$. Dashed lines: $\hat{v}$-T relation in the low-rate limit as reconstructed using the limiting glass and rubber $\hat{v}$-T slopes with the experimental density at 300 K (solid circle). b) $\hat{v}$-$\dot{q}$ for each composition ϕ_{ENB} at 300 K. c) The ratio of void volume to total volume v_v/v_0 for $\dot{q}$ and ϕ_{ENB} at 300 K. Solid lines: fits to a time-temperature superposition of the form $v_v(\dot{q}) = A + B(-c_2 \log(\dot{q}_0/\dot{q})/(c_1 + \log(\dot{q}_0/\dot{q})))$ with A and B as free parameters, $\dot{q}_0 = 10^0$ K/s, and $c_1 = 15$ and $c_2 = 50$. d) The mean-square displacement of atoms $\langle \Delta r^2 \rangle$ over time t and composition ϕ_{ENB} for a representative cooling rate ($\dot{q} = 10^0$ K/s) at 300 K. The Debye-Waller factor $\langle u^2 \rangle$ in the simulations is taken as $\langle \Delta r^2 (t = 1ps) \rangle$.[13–15] Values of $\langle u^2 \rangle$ from neutron scattering experiments with $\phi_{ENB} = 0.0$, 0.5, and 1.0 are shown for comparison (dashed lines). e) Atomic mean-square displacement $\langle \Delta r^2 \rangle$ vs. time t and cooling rate $\dot{q}$ for a representative composition ($\phi_{ENB} = 0.5$) at 300 K. f). The Debye-Waller factor vs void fraction at 300 K given as a log-log plot. Dashed lines: fits to a power law given in Eq. 1; solid black lines indicate limiting slopes of $\alpha = 3$ (upper black line) and $\alpha = 1$ (lower black line); an intersection point (large solid circle) is assumed for large v_v/v_0.

where α is in the range 1 to 3, corresponding to cylindrical tunnels and spherical cavities, respectively.[26] From the above, a compact localization model that accounts for the structure of the free volume can be written as $\tau = \tau_0 \exp\left[(u_0^2/\langle u^2 \rangle)^{\alpha/2}\right]$. With this in mind, we probe the structural relaxation of ENB-NBOH polymers using the Debye-Waller factor as a proxy. (We note that τ can be directly found by estimating the parameters τ_0 and u_0^2 though analysis of $\langle u^2(T) \rangle$ for each composition.[14]; τ_0 and u_0^2 are treated as constants over the composition range given here.) Molecular simulations were carried out to characterize the specific volume, void volume, and fast dynamics as a function of the fraction of non-polar monomers and quench rate. These results are summarized in Figure 3. From Figure 3a and 3b, it is clear that either increasing the quench rate or increasing the fraction of non-polar ENB monomers expands the volume. Similarly, Figure 3c shows that the fractional volume of voids, as analyzed from clustering analysis, increases with ENB fraction and quench rate. As expected, the Debye-Waller factor and overall MSD increase with ENB fraction and with quench rate, as given in Figures 3d and 3e. Further, the trend of increasing $\langle u^2 \rangle$ with ϕ_{ENB} is confirmed by QENS measurements, with excellent numerical agreement observed for $\phi_{ENB} = 0$ and 0.5. (Additional MSD data and analysis details for simulations and QENS are given in Fig. S3 and Figs. S5-S9 of the ESI.)

We now compare the void volumes with the Debye-Waller factor. From Figure 3f, it is clear that the four glass preparations examined here have different relationships between the dynamics and void volume, which we take here as a stand in for the free volume. A numerical fit of $\langle u^2 \rangle$ for each quench to Eq. 1 indicates values of α in the range 1.7-3.0, with the relatively slow quenched systems having lower values that suggest spherical-like cavities whereas the fast quenches have higher values. Interestingly, the free volume of the polymer compositions are significantly overlapping, with many of the polar compositions formed at fast quench rates having values similar to less polar compositions at slower quenches. Despite these similarities, the Debye-Waller factor of the fast quench systems does not increase as rapidly as would be expected with changes to the ENB composition. In general, the data indicate that similar free volumes do not give similar Debye-Waller factors across quench rates, with a stronger mismatch oc-

curring for slower quenches where the free volume is relatively low.

These differences can be attributed in part to the differing structure of the free volume, as measured by the geometry of voids. An analysis of the void volumes and their relative shape anisotropy (RSA) is shown in Figure 4. The histogram shows that many small voids have a spherical-like character, and particularly so for the densest systems ($\dot{q} = 10^0$ K/s) where α is near three. However, as the quench rate becomes faster (observed by moving from the bottom to top of each column), the presence of large voids with high asymmetries is greatly increased. Given the shift in the size and shape of voids, its seems unlikely that a fixed value of α can describe the dynamics across quench rates. While the quench rates used here are not experimentally viable, the results can be interpreted more generally as an instance of glass processing that adds free volume to the structure. This result suggests that measures of the free volume do have the potential to represent glass dynamics for limited ranges of compositions like those in many systematic studies, however the predictive power is lost if the similar structure of the free volume is broken by changes in processing conditions. Further, the results here clearly demonstrate that molecular simulations of the same glass composition can capture a wide range of meta-stable structures, each with differing dynamics, and each with differing trends in the dynamics as the composition is altered. Thus, going forward, a clear understanding of packing and its relationship with dynamical properties is needed if molecular simulations are to take a more predictive role in materials design.

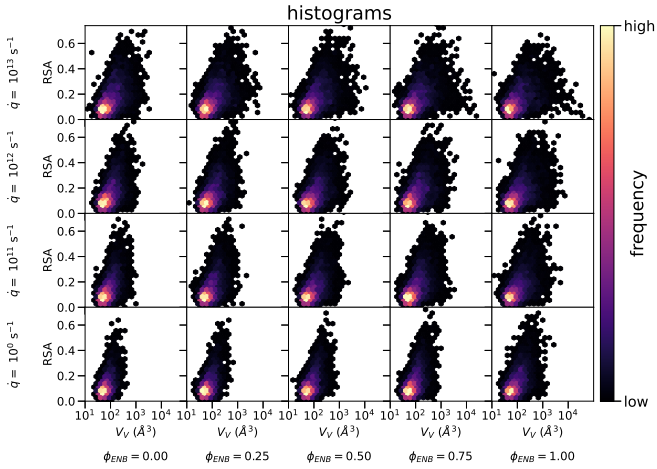

Fig. 4 Frequency of voids for various sizes $\langle V_v \rangle$ and relative shape anistropy RSA. Plots are shown across four quench rates (columns) and across five ENB fractions (rows).

Conflicts of interest

There are no conflicts to declare.

Acknowledgements

The U.S. Government is authorized to reproduce and distribute reprints for government purposes notwithstanding any copyright notation hereon. A.K. acknowledges finacnical assistance from the U.S. Department of Commerence, National Institute of Standards and Technology (Award 70NANB15H272).

Notes and references

1 R. M. Elder, D. B. Knorr, J. W. Andzelm, J. L. Lenhart and T. W. Sirk, *Soft Matter*, 2016, **12**, 4418–4434.
2 R. M. Elder, T. R. Long, E. D. Bain, J. L. Lenhart and T. W. Sirk, *Soft Matter*, 2018, **14**, 8895–8911.
3 Y. Qiu, L. W. Antony, J. M. Torkelson, J. J. De Pablo and M. Ediger, *The Journal of Chemical Physics*, 2018, **149**, 204503.
4 K. M. Salerno, J. L. Lenhart, J. J. de Pablo and T. W. Sirk, *The Journal of Physical Chemistry B*, 2020, **124**, 6112–6120.
5 J. M. Dennis, T. R. Long, A. Krishnamurthy, N. T. Tran, B. A. Patterson, C. E. Busch, K. A. Masser, J. L. Lenhart and D. B. Knorr Jr, *ACS Applied Polymer Materials*, 2020, **2**, 2414–2425.
6 C. L. Soles, F. T. Chang, B. A. Bolan, H. A. Hristov, D. W. Gidley and A. F. Yee, *Journal of Polymer Science Part B: Polymer Physics*, 1998, **36**, 3035–3048.
7 M. Eldrup, D. Lightbody and J. N. Sherwood, *Chemical Physics*, 1981, **63**, 51–58.
8 A. Krishnamurthy, R. Tao, E. Senses, S. M. Doshi, F. A. Burni, B. Natarajan, D. Hunston, E. T. Thostenson, A. Faraone, A. L. Forster *et al.*, *ACS applied polymer materials*, 2019, **1**, 1905–1917.
9 T. Kajitani, K. Shibata, S. Ikeda, M. Kohgi, H. Yoshizawa, K. Nemoto and K. Suzuki, *Physica B: Condensed Matter*, 1995, **213**, 872–874.
10 M. Ester, H.-P. Kriegel, J. Sander and X. Xu, Proceedings of the Second International Conference on Knowledge Discovery and Data Mining, 1996, pp. 226–231.
11 F. Pedregosa, G. Varoquaux, A. Gramfort, V. Michel, B. Thirion, O. Grisel, M. Blondel, P. Prettenhofer, R. Weiss, V. Dubourg, J. Vanderplas, A. Passos, D. Cournapeau, M. Brucher, M. Perrot and E. Duchesnay, *J. Mach. Learn. Res.*, 2011, **12**, 2825–2830.
12 D. Račko, R. Chelli, G. Cardini, S. Califano and J. Bartoš, *Theoretical Chemistry Accounts*, 2007, **118**, 443–448.
13 L. Larini, A. Ottochian, C. De Michele and D. Leporini, *Nature Physics*, 2007, **4**, 42.
14 B. A. Pazmiño Betancourt, P. Z. Hanakata, F. W. Starr and J. F. Douglas, *Proceedings of the National Academy of Sciences*, 2015, **112**, 2966.
15 D. M. Saylor, S. Jawahery, J. S. Silverstein and C. Forrey, *The Journal of Chemical Physics*, 2016, **145**, 031106.
16 L. Li and A. F. Yee, *Macromolecules*, 2003, **36**, 2793–2801.
17 J. Liu and A. F. Yee, *Macromolecules*, 2000, **33**, 1338–1344.
18 C. L. Soles, A. B. Burns, K. Ito, E. Chan, J. Liu, A. F. Yee and M. S. Tyagi, *Macromolecules*, 2020, **53**, 6672–6681.
19 C. L. Soles, A. B. Burns, K. Ito, E. P. Chan, J. F. Douglas, J. Wu, A. F. Yee, Y.-T. Shih, L. Huang, R. M. Dimeo *et al.*, *Macromolecules*, 2021, **54**, 2518–2528.
20 L. A. Gray and C. B. Roth, *Soft Matter*, 2014, **10**, 1572–1578.
21 A. N. Raegen, J. Yin, Q. Zhou and J. A. Forrest, *Nature Mate-*

rials, 2020, 1–4.

22 Y. Guo, A. Morozov, D. Schneider, J. W. Chung, C. Zhang, M. Waldmann, N. Yao, G. Fytas, C. B. Arnold and R. D. Priestley, *Nature materials*, 2012, **11**, 337–343.

23 D. Turnbull and M. H. Cohen, *The Journal of chemical physics*, 1961, **34**, 120–125.

24 R. W. Hall and P. G. Wolynes, *The Journal of chemical physics*, 1987, **86**, 2943–2948.

25 F. W. Starr, S. Sastry, J. F. Douglas and S. C. Glotzer, *Physical review letters*, 2002, **89**, 125501.

26 D. S. Simmons, M. T. Cicerone, Q. Zhong, M. Tyagi and J. F. Douglas, *Soft Matter*, 2012, **8**, 11455–11461.

Soft Matter

ARTICLE TYPE

Cite this: DOI: 00.0000/xxxxxxxxxx

Electronic Supplemental Information for "Relative effects of polymer composition and sample preparation on glass dynamics"

Robert M. Elder[a*], Amanda L. Forster[b], Ajay Krishnamurthy[b], Joseph M. Dennis[c], Hiroshi Akiba[d], Osamu Yamamuro[d], Kanae Ito[e], Katherine M. Evans[f], Christopher Soles[f], Timothy W. Sirk[c*]

Received Date
Accepted Date

DOI: 00.0000/xxxxxxxxxx

1 Additional Simulation Details

Composition. The simulated polymers were built from ENB and NBOH repeat units. The least polar chemistry is pure ENB with 20 ENB monomers per chain. From there, we increased the polarity by replacing 5, 10, 15, or all 20 of the ENB monomers with NBOH. These ENB-*co*-NBOH copolymers are termed $\phi_{ENB} = 100$, 75, 50, 25, 0% ENB, respectively. The monomers were randomly distributed along the chains. For each copolymer, five chains with distinct random ordering were generated. We packed 64 of each distinct chain into the simulation cell to create a large system with 320 chains. These systems contained exactly 136,000 atoms, a relatively large volume compared with the void volumes of interest. As in prior work,[1–3] we quantified the polarity via the octanol-water partition coefficient $\log P$ normalized by molecular surface area SA. Low $\log P/SA$ indicates high hydrophilicity or polarity.

Forcefield and equation of motion. The general Amber force field (GAFF, version 2.1) was used for all systems.[4,5] Short-range non-bonded interactions were cut off at 9 Å, and long-range contributions of van der Waals interactions to the energy and pressure were estimated using tail corrections.[6] Atomic partial charges were calculated using the AM1-BCC method.[7,8] Electrostatic interactions were calculated using the particle-particle particle-mesh (PPPM) method.[9] The velocity-Verlet integrator was used with a timestep of 1.0 fs. Temperature and pressure were controlled with a Nosé-Hoover thermostat and barostat with damping constants of 0.1 and 1.0 ps, respectively.[10] Isotropic pressure control was used to maintain 1 atm pressure. The simulation box was periodic in three dimensions. We employed the LAMMPS simulation package[11] (http://lammps.sandia.gov) for all simulations. VMD was used for visualization.[12]

Sample preparation. After construction, the systems were equilibrated with isothermal-isobaric (*NPT*) MD simulation at 700 K for 1 ns. The structures were then slowly relaxed into the glassy state using incremental cooling. The temperature was reduced in steps of 20 K, with a short *NPT* MD simulation performed at each new temperature, until the system was in the glassy state at 300 K. The duration of the short *NPT* MD simulation was chosen to set the cooling rate: 200 ps for 10^{11} K/s, 20 ps for 10^{12} K/s, and 2 ps for 10^{13} K/s. Five replica structures were created for each chemistry, using different initial positions and velocities such that the replicas have different structures. Error bars are the standard deviation of these five replicas. Molecular structures were generated at the experimental density via hydrostatic compression after the initial quench to 300 K, as follows: starting from structures quenched at 10^{11} K/s, the box volume was affinely scaled to the experimental density over 1 ns. We term this protocol 'quench-then-compress' (QtC), which is referred to as $\dot{q} = 10^0$ K/s in the manuscript. To verify that the void volume distribution is not overly sensitive to this protocol, we also performed the opposite 'compress-then-quench' (CtQ). In CtQ, the system is scaled to the correct density at high T and then quenched to 300 K at 10^{11} K/s. The void distributions in the final structure were similar. Full distributions are shown in Figure S1.

[a]*current address: Center for Devices and Radiological Health, U.S. Food and Drug Administration, Silver Spring, Maryland 20903, United States; E-mail: robert.elder@fda.hhs.gov*
[b]*Materials Measurement Science Division, National Institute of Standards and Technology, Gaithersburg, Maryland 20899, United States*
[c]*Polymers Branch, U.S. DEVCOM Army Research Laboratory, Aberdeen Proving Ground, Maryland 21005, United States; E-mail: timothy.w.sirk.civ@army.mil*
[d]*Institute for Solid State Physics, University of Tokyo, Kashiwa, Chiba, 277-8581, Japan*
[e]*Industrial Application Division, Spring-8, Japan Synchrotron Radiation Research Institute (JASRI), 1-1-1 Kouto, Sayo, Hyogo 679-5198, Japan*
[f]*Materials Science and Engineering Division, National Institute of Standards and Technology, Gaithersburg, Maryland 20899, United States*

Additional results. Distributions of void volume from the simulations are given for all quench rates and compositions in Figure S2. Similarly, all MSD curves from simulations are provided in Figure S3, where $\langle \Delta r^2(t) \rangle$ is computed by averaging over the self-diffusion for each atom i as

$$\langle \Delta r^2(t) \rangle = \left\langle \left[r_i(t_0+t) - r_i(t_0) \right]^2 \right\rangle. \quad (1)$$

The MSD curves shown in Fig. S3 and results given in the main text are averaged over all replica structures and reference times t_0.

Figure S4 shows a comparison of void volume distributions for systems with varying composition and quench rate but with similar average void volumes. The distributions are generally similar for small voids. Figure S5 shows a comparison between the Debye-Waller factor $\langle u^2 \rangle$ obtained from simulations and experiments for $\phi_{ENB} = 0.0$, 0.5, and 1.0. Figure S6 gives an example calculation of α at 500 K ($T \gg T_g$).

2 Additional Experimental Details

Quasi-elastic neutron scattering (QENS) measurements were performed on the angle focusing neutron spectrometer, AGNES, on the cold neutron guide (C3-1-1) at the Japan Atomic Energy Agency's Japanese Research Reactor 3 (JRR-3).[13] This cold neutron time-of-flight spectrometer, a part of the University of Tokyo's Institute for Solid State Physics, was operated in the "high resolution mode," selecting a neutron wavelength of 5.5 Å, which corresponds to an elastic peak energy resolution of 0.04 meV at full width half max. Given this energy resolution, relaxation processes longer than approximately 10 ps appear static. At these settings the AGNES spectrometer can nominally access a Q range of approximately (0.15 to 2.1) Å^{-1}. Full inelastic neutron scattering spectra were collected at 8 hours per spectrum for the following samples and temperatures (K):

ϕ_{ENB} = 1.0: 4, 100, 150, 200, 250, 300, 350
ϕ_{ENB} = 0.5: 100, 200, 300
ϕ_{ENB} = 0.0: 4, 100, 150, 200, 250, 300, 350

In this publication we limit our analysis of the QENS spectra to the elastic scattering intensities to quantify a mean-square atomic displacement, $\langle u^2 \rangle$, that can be compared to the molecular dynamics simulations presented in the main text of this manuscript. At these low temperatures, the elastic scattering intensities (IE) were relatively weak and did not warrant breaking the QENS spectra into multiple bins of Q. Rather than the conventional plotting of $\log(I_{el})$ vs Q^2 to extract $\langle u^2 \rangle$ at each T from the slope, we integrated the values of I_E over all of the available Qs into $I_{E-total}$. We then plot the relative mean square displacements in terms of $\langle u^2(T) \rangle - \langle u^2(5K) \rangle$ from $[\log(I_{E-total}(T)) - \log(I_{E-total}(5K))]/Q^2_{ave}$ where $Q^2_{ave} \approx 1.0$ Å^{-1}.

Figure S7 below shows an example of the elastic peaks in the QENS data as a function of temperature for the ϕ_{ENB}=1.0 resin. Data for the ϕ_{ENB}= 0.5 and 0.0 resins are qualitatively similar and not shown here. The vertical lines between -0.14 and +0.08 meV give the energy limits over which the IE was integrated. Figure S8 then correspondingly shows how $I_{E-total}$ varies across the different temperatures and compositions studied. The intensity variation among the three samples is due to the difference in sample quantity. These values were then used to calculate the relative mean square displacement, $\langle u^2(T) \rangle - \langle u^2(5K) \rangle$, as a function of T, as shown in Figure S9. The $\langle u^2(T) \rangle - \langle u^2(5K) \rangle$ at 300 K are taken from this plot and overlaid onto Figure 3d in the main portion of the manuscript. The $\langle u^2 \rangle$ values of the sample with $\phi_{ENB} = 1.0$ are smaller than expected at higher temperatures. This may be because the Q region for the integration is limited to 0.5-2.1 Å^{-1}. That is, the spatial range for the motion of the sample with $\phi_{ENB} = 1.0$ may spread, especially to the low-Q region. Given the energy resolution of the spectrometer, it is important to realize that $\langle u^2(T) \rangle - \langle u^2(5K) \rangle$ integrates motions that are faster than 10 ps, but with an emphasis on the lower frequency motions in the integral. In the fullest representation for the harmonic vibrations in a crystal, $\langle u^2 \rangle$ in a neutron scattering experiment is a frequency weighted integral over the vibrational density of states within the sample:

$$\langle u^2 \rangle = \frac{3\hbar}{2M} \int_0^{\omega_m} \frac{1}{\omega} \coth\left(\frac{1}{2}\omega\beta\right) Z(\omega) d\omega \quad (2)$$

In this equation, $Z(\omega)$ is the phonon density of states in the sample as a function of frequency of motion ω, M is the molar mass, and β is $1/k_bT$.[14] When this integration is performed, we find that the frequency dependence of $\langle u^2 \rangle$ reduces to:

$$\langle u^2 \rangle \sim \frac{Z(\omega)}{\omega^2} \quad (3)$$

This illustrates that the lowest frequency motions in the system dominate $\langle u^2 \rangle$, which makes intuitive sense. High frequency (energy) motions tend to be more localized, with small displacements, in comparison to low frequency (energy) motions that tend to be more extensive and delocalized. Therefore it is reasonable to expect that the motions reflected in $\langle u^2(T) \rangle - \langle u^2(5K) \rangle$ are dominated by the slowest 10 ps motions that can be resolved by the AGNES spectrometer.

Notes and references

1 R. M. Elder, T. R. Long, E. D. Bain, J. L. Lenhart and T. W. Sirk, *Soft Matter*, 2018, **14**, 8895–8911.
2 A. J. D. Magenau, J. A. Richards, M. A. Pasquinelli, D. A. Savin and R. T. Mathers, *Macromolecules*, 2015, **48**, 7230–7236.
3 E. Yildirim, D. Dakshinamoorthy, M. J. Peretic, M. A. Pasquinelli and R. T. Mathers, *Macromolecules*, 2016, **49**, 7868–7876.
4 J. Wang, R. M. Wolf, J. W. Caldwell, P. A. Kollman and D. A. Case, *J. Comput. Chem.*, 2004, **25**, 1157–1174.
5 J. Wang, W. Wang, P. A. Kollman and D. A. Case, *J. Mol. Graphics Modell.*, 2006, **25**, 247–260.
6 H. Sun, *J. Phys. Chem. B*, 1998, **102**, 7338–7364.
7 A. Jakalian, B. L. Bush, D. B. Jack and C. I. Bayly, *J. Comput. Chem.*, 2000, **21**, 132–146.
8 A. Jakalian, D. B. Jack and C. I. Bayly, *J. Comput. Chem.*, 2002, **23**, 1623–1641.

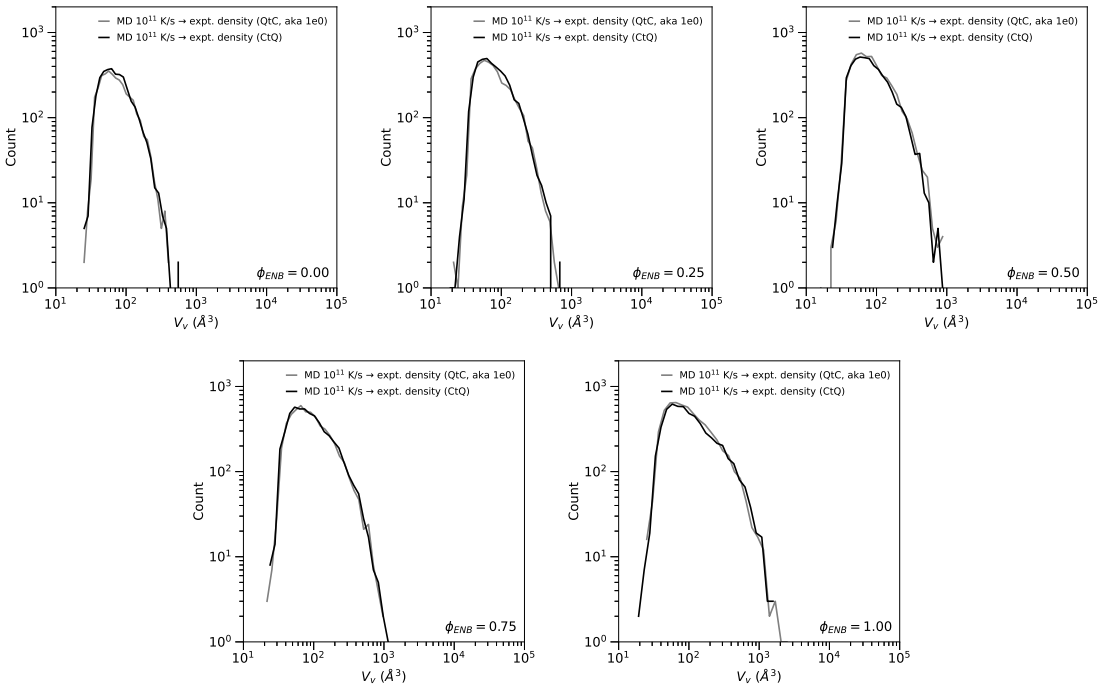

Fig. S1 Void volume $\langle v_v \rangle$ distributions from simulations for all compositions ϕ_{ENB} and using the QtC (i.e., $\dot{q} = 10^0$ K/s in the manuscript) and CtQ protocols with a quench rate of 10^{11} K/s and the target density chosen to match the experimental value.

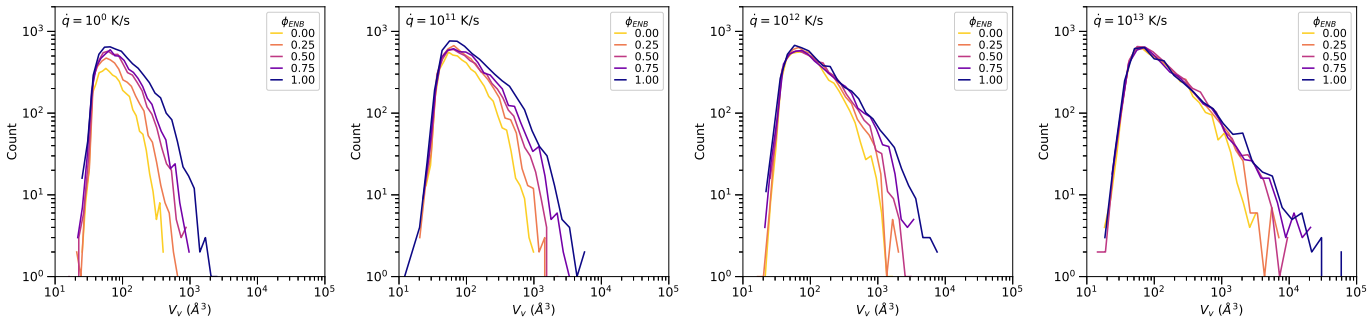

Fig. S2 Void volume $\langle v_v \rangle$ distributions from simulations for all compositions ϕ_{ENB} and quench rates $\dot{q}$.

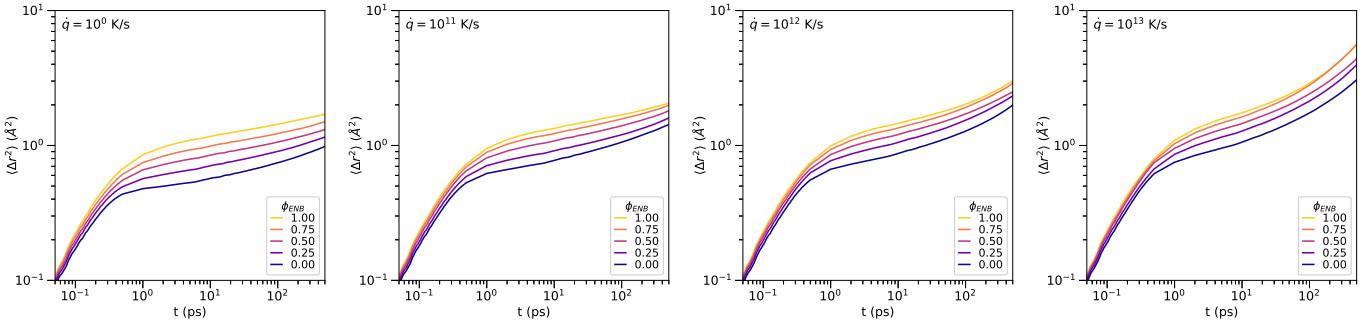

Fig. S3 Mean-squared displacements $\langle \Delta r^2 \rangle$ from simulations for all compositions ϕ_{ENB} and quench rates $\dot{q}$.

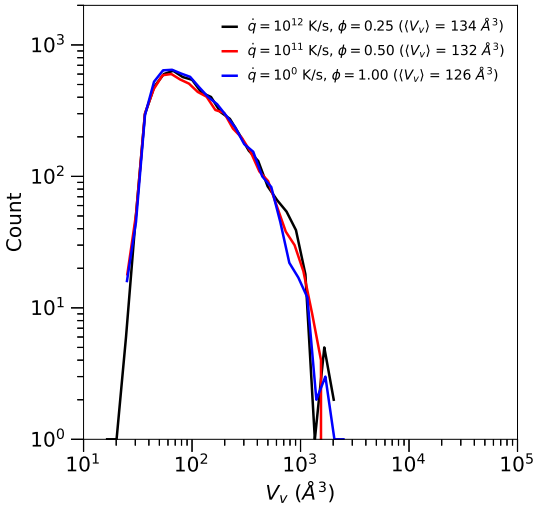

Fig. S4 Comparison of void volume $\langle v_v \rangle$ distributions from simulations with compositions ϕ_{ENB} and quench rates $\dot{q}$ with similar average void volume $\langle V_v \rangle$.

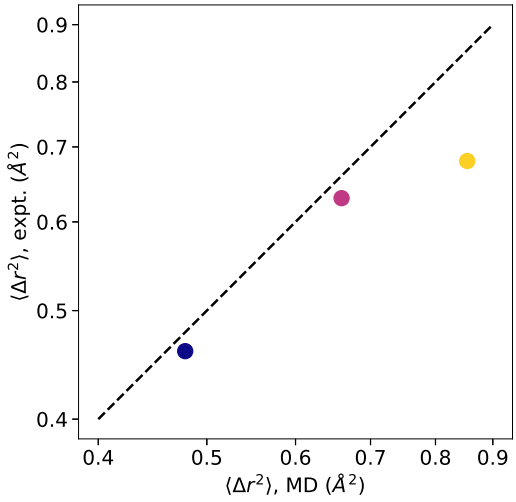

Fig. S5 Comparison of the Debye-Waller factor $\langle u^2 \rangle$ obtained from simulations and experiments for $\phi_{ENB} = 0.0$, 0.5, and 1.0. The dashed line indicates equality between the x and y axes.

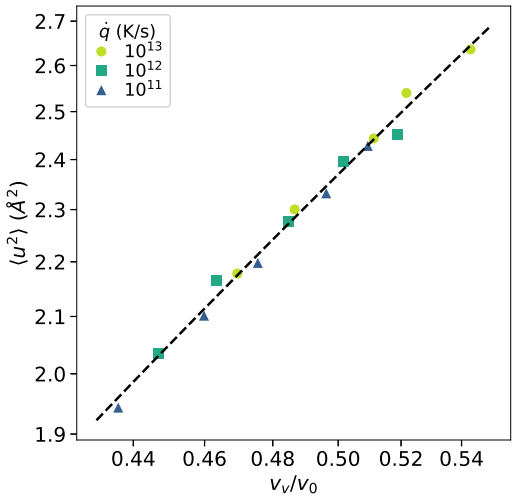

Fig. S6 The Debye-Waller factor vs void fraction at 500 K ($T >> T_g$), given as a log-log plot. The dashed line is a fit to a power law $\langle u^2 \rangle \sim (v_v/v_0)^{2/\alpha}$ with the exponent $\alpha \approx 3/2$.

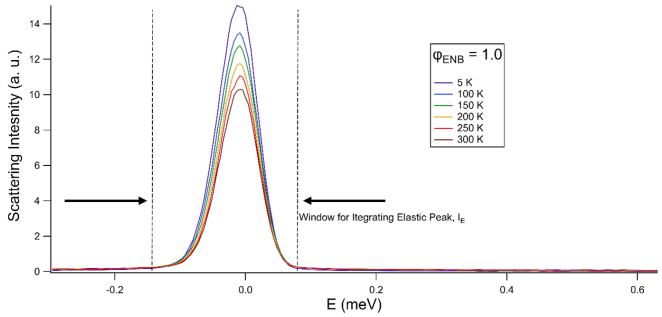

Fig. S7 Full QENS spectra as a function of T for the $\phi_{ENB} = 0.0$ sample. Vertical lines indicate the limits over which the strong central elastic peak intensities were integrated.

9 R. W. Hockney and J. W. Eastwood, *Computer simulation using particles*, Institute of Physics Publishing, Philadelphia, 1988, p. 564.

10 W. Shinoda, M. Shiga and M. Mikami, *Phys. Rev. B*, 2004, **69**, 134103.

11 S. Plimpton, *J. Comput. Phys.*, 1995, **117**, 1–19.

12 W. Humphrey, A. Dalke and K. Schulten, *J. Mol. Graphics*, 1996, **14**, 33–38.

13 T. Kajitani, K. Shibata, S. Ikeda, M. Kohgi, H. Yoshizawa, K. Nemoto and K. Suzuki, *Physica B: Condensed Matter*, 1995, **213**, 872–874.

14 G. Squires, *Introduction to the Theory of Thermal Neutron Scattering by GL Squires*, 1996.

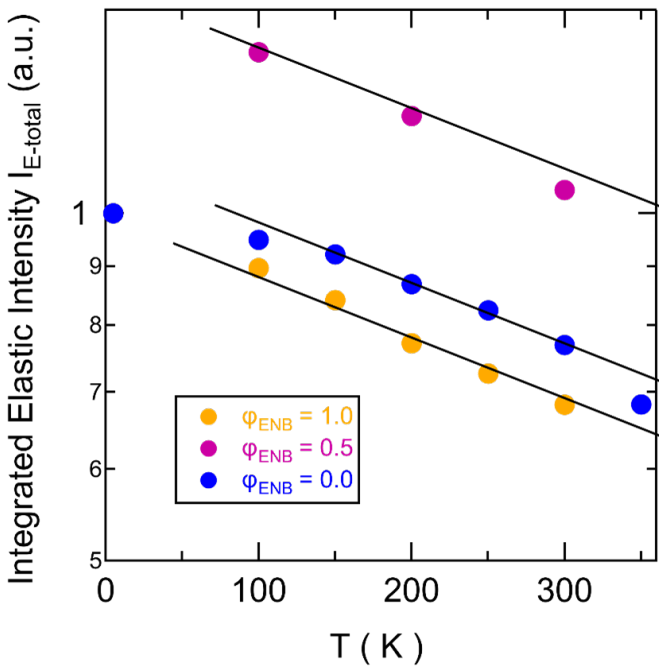

Fig. S8 Integrated total elastic peak intensities $I_{E-total}$ for the different ENB compositions ϕ_{ENB} and temperatures T studied here. Straight lines are simple guides to the eye.

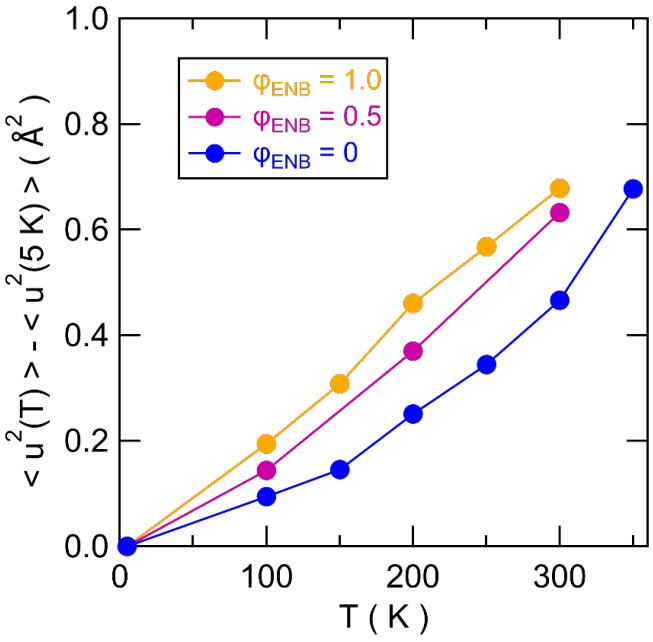

Fig. S9 Relative mean-square displacements $\langle u^2(T)\rangle - \langle u^2(5K)\rangle$ for the different ENB compositions ϕ_{ENB} and temperatures T studied here.